Available online at www.sciencedirect.com
ScienceDirect
Deep-Sea Research I 54 (2007) 269–291
DEEP-SEA RESEARCH PART I
www.elsevier.com/locate/dsri

Experimental studies of rotating exchange flow

B. Rabe[a,*], D.A. Smeed[a], S.B. Dalziel[b], G.F. Lane-Serff[c]

[a]National Oceanography Centre, Southampton, UK
[b]DAMTP, University of Cambridge, UK
[c]School of Mechanical, Aerospace and Civil Engineering, University of Manchester, UK

Received 19 August 2005; received in revised form 8 November 2006; accepted 20 November 2006
Available online 23 January 2007

Abstract

Ocean basins are connected by straits and passages, geometrically limiting important heat and salt exchanges which in turn influence the global thermohaline circulation and climate. Such exchange can be modeled in an idealized way by taking into consideration the density-driven two-layer flow along a strait under the influence of rotation. We use a laboratory model of a lock exchange between two reservoirs of different density through a flat-bottom channel with a horizontal narrows, set up on two different platforms: a 1 m diameter turntable, where density interface position was measured by dye attenuation, and the 14 m diameter turntable at Coriolis/LEGI (Grenoble, France), where correlation imaging velocimetry, a particle imaging technique, allowed us to obtain for the first time detailed measurements of the velocity fields in these flows. The influence of rotation is studied by varying a parameter, B_u, a type of Burger number given by the ratio of the Rossby radius to the channel width at the narrows. In addition, a two-layer version of the Miami Isopycnic Coordinate Model (MICOM) is used, to study the cases with low Burger number. Results from experiments by Dalziel [1988. Two-layer hydraulics: maximal exchange flows. Ph.D. Thesis, Department of Applied Mathematics and Theoretical Physics, University of Cambridge, see also ⟨http://www.damtp.cam.ac.uk/lab/people/sd103/papers/1988/Thesis_Dalziel.pdf⟩] are also included for comparison. Time-mean exchange fluxes for any B_u are in close agreement with the inviscid zero-potential vorticity theory of Dalziel [1990. Rotating two-layer sill flows. In: Pratt, L.J. (Ed.), The Physical Oceanography of Sea Straits. Kluwer Academic, Dordrecht, pp. 343–371] and Whitehead et al. [1974. Rotating hydraulics of strait and sill flows. Geophysical Fluid Dynamics 6, 101–125], who found that fluxes for $B_u > 1$ mainly vary with channel width, similar to non-rotating flow, but for $B_u < 1$ are only limited by the Rossby radius. We also show theoretically that non-zero-potential vorticity results in only a small increase in the predicted exchange flux around $B_u \sim 1$. The flow characteristics are found to be very different for small and large Burger numbers: for $B_u > 1$ a steady, two-layer flow was observed that persisted across the channel at the narrows with only some across-channel variation. The distribution of the Froude number is found to give some evidence for hydraulic control in a manner similar to that of non-rotating flows under the influence of bottom drag. Flow for $B_u < 0.5$ does not appear to reach a steady state but instead is characterized by an unsteady, meandering current and several eddies in the strait. Similar instabilities also occur in wide oceanic straits, where several mechanisms, such as barotropic and baroclinic instability, have been proposed and could also be one cause of time variability in our experiments. Both the laboratory experiments and the MICOM results suggest that in the

*Corresponding author. AWI for Polar and Marine Science, Bussestr. 24, Postfach 120161, 27515 Bremerhaven, Germany. Tel.: +49 471 4831 2403; fax: +49 471 4831 1797.
E-mail address: brabe@awi-bremerhaven.de (B. Rabe).

0967-0637/$ - see front matter
doi:10.1016/j.dsr.2006.11.002

presence of bottom drag or side wall friction some features of the flow, such as the location of the channel crossing, become sensitive to the initial conditions. These effects differ in flows with $B_u > 1$ and $B_u < 1$.

Keywords: Rotation; Exchange; Strait; Experiment; Two-layer; Hydraulic control

1. Introduction

Ocean basins and marginal seas are connected by straits and passages. Many such passages are associated with heat and fresh-water fluxes crucial to the thermohaline circulation, and hence climate. One well-known example is the Strait of Gibraltar (e.g. Bryden et al., 1994; Astraldi et al., 1999), where water from the North Atlantic exchanges with salty Mediterranean water. The outflow from the Mediterranean has a significant effect on the properties and circulation of the North Atlantic (e.g. Reid, 1994; Jia, 2000). However, many ocean general circulation models (OGCMs) cannot accurately resolve exchange flows (Bigg et al., 2003), requiring instead a suitable parametrization.

Due to this need for parametrization, much attention has been given to the physics of exchange flows. Most theoretical studies have assumed that exchange is governed by the process of hydraulic control (Armi, 1986; Dalziel, 1991). According to these theories, long baroclinic gravity waves are arrested at control locations, usually associated with a topographic constriction, such as a horizontal narrows or a sill. If the flow is fully hydraulically controlled, no such waves can propagate into the control regions from the reservoirs. For many straits the width is similar to or wider than the baroclinic Rossby deformation radius, and so the effects of rotation must be considered. Examples of such straits include the Strait of Sicily (Beranger et al., 2004; Stansfield et al., 2003, 2001) and the straits connecting the North Atlantic to the Nordic Seas (Pratt, 2004).

There have been a number of studies of single-layer rotating overflows, but relatively few theoretical studies of two-layer rotating exchange flows (see Pratt, 2004 for a review). In these studies the steady shallow-water equations are usually subjected to a semi-geostrophic approximation with the assumption of small along-channel variations and small cross-channel velocities relative to the corresponding along-channel variables. In this context, Whitehead et al. (1974) used simple theoretical arguments to derive a maximal exchange flux for flows with zero-potential vorticity. Using along-channel geostrophic balance and energy conservation, Hunkins and Whitehead (1992) predicted the flux for exchange flows with constant but non-zero-potential vorticity for one value of the Burger number at which interface was close to separating from the side walls. Dalziel (1990) derived a hydraulic functional for two-layer flow, similar to that used for single-layer flows by Gill (1977). Dalziel (1990) used the functional approach to determine the flux for several strait geometries. As in the non-rotating case, Dalziel's maximal exchange flux is associated with fully controlled flows. This was also found in theoretical studies for hydraulic exchange flows through arbitrary strait topography by Killworth (1995), who concluded that maximal flux can only occur in fully hydraulically controlled exchange flows.

None of these theories take into account issues, that have been studied for non-rotating exchange flows, such as time-dependence (Helfrich, 1995) or friction (Hogg et al., 2001; Zaremba et al., 2003; Winters and Seim, 2000). While the latter has, to some extent, been described in the context of secondary Ekman circulation in oceanic flows (Johnson and Ohlsen, 1994), complicated topography makes an accurate estimate of these effects difficult.

Another difficulty with the theory, highlighted by Dalziel (1990) and Riemenschneider et al. (2005), is that of flow reversal. For Burger numbers, here defined as the ratio of the Rossby radius to the width of the strait, less than about one, the solutions of Riemenschneider et al. (2005) exhibited backflow at the control section. Note that the backflow only occurred at locations where one of the layers was separated from one of the side walls of the channel. Within regions of backflow it is not possible to assume that all of the flow originates in the upstream reservoir, and hence flow properties such as potential vorticity and Bernoulli potential cannot be determined unambiguously. Dalziel (1990) avoided this problem by excluding backflow and making these regions stagnant, but this is not necessarily correct for real flows. Another theory by

Pratt and Armi (1990) assumed that the baroclinic flow is limited to boundary layers near the side walls with uniform barotropic shear present throughout the channel. However, their theory breaks down for flows where the interface is separated from one or both side walls and flows where the reservoir depths are equal.

Experimental work has given great insight into rotating exchange flow processes. For example, Whitehead et al. (1974) used a rectangular channel connecting deep basins to simulate a lock-exchange with zero-potential vorticity, whereas Whitehead and Miller (1979) and Hunkins and Whitehead (1992) both used constant water depth throughout with a channel of variable width connecting two reservoirs. Whitehead and Miller (1979) showed highly unstable flow and eddies for low Burger numbers, but focused their analysis on the circulation within the reservoirs. Hunkins and Whitehead (1992) found good agreement of measured exchange fluxes with their finite potential vorticity theory for one value of the Burger number. Similar experiments by Dalziel (1988) in a variable width channel with a flat-bottom and finite depth reservoirs showed good agreement with fluxes predicted by his theory. However, perhaps because of frictional effects (see also Johnson and Ohlsen, 1994) none of these experiments clearly showed flow separation at the narrows, although Dalziel (1988) did observe a distinct channel crossing of the currents in the vicinity of the narrows. Where flow separation did occur, the lack of velocity measurements made it difficult to determine the circulation within the separated region. The lack of velocity measurements also made it difficult to see the time-variability in the flow fields.

In this paper we present an experimental study of rotating exchange flow through a flat-bottom channel with a horizontal narrows. Experiments were performed on both a small (a 1 m diameter rotating table) and a large (the 14 m Coriolis table in Grenoble) platform allowing a range of Ekman numbers to be considered. Three-dimensional fields of the horizontal velocity were measured on the large platform, and interface height fields and flux measurements were obtained in both sets of experiments.

The experimental setups are described in the following section, and the results are presented in Section 3. It will be shown that our measurements of the exchange flux compare well with semi-geostrophic hydraulics theory (described in Appendix D) and previously unpublished experiments by Dalziel (1988). However, where the internal Rossby radius is significantly less than the channel width at the narrows the flow is found to be unsteady. Furthermore, significant asymmetries between the two exchanging layers are found. The relationship between this asymmetry and the frictional boundary layers and initial conditions is examined in Section 4 where comparisons are made with numerical simulations using the Miami isopycnic coordinate model (MICOM).

2. Experimental method

2.1. Layout and scaling

In both sets of experiments a flat-bottom channel of length L, with a rectangular cross-section and a horizontal constriction of minimum width W, connects two reservoirs. These reservoirs are initially well-mixed, with density difference $\Delta\rho$ and a mean density of $\bar{\rho}$ (Fig. 1). The reservoirs are initially separated by a barrier, usually located at the end of the channel closest to the reservoir holding the denser fluid. Throughout this paper, the $y<0$ and $y>0$ sides of the channel will be referred to as "RHS" and "LHS" or the "right-hand" and "left-hand" part of the channel, as if facing the light reservoir.

The Rossby radius is defined to be $R=\sqrt{g'H}/f$, where $f=4\pi/T$ is the Coriolis parameter based on

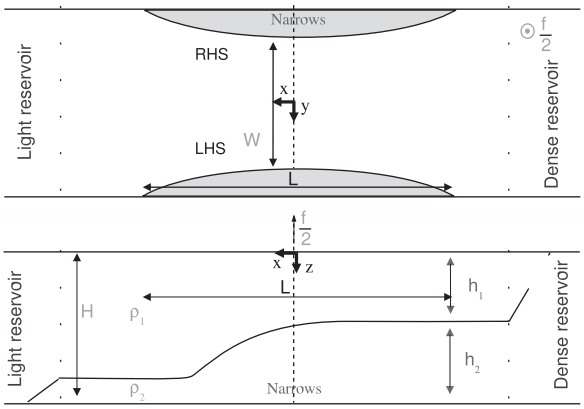

Fig. 1. Schematic diagram of experimental setup. The coordinate origin is in the center of the channel at the surface with x increasing along-channel toward the light reservoir, y across-channel to the left (LHS) and z vertically downward. $h_{1(2)}$ and $\rho_{1(2)}$ are the upper (lower) layer depth and density, respectively, and H the total water depth. W is the total channel width at the narrows and L the length of the channel. The barrier (not shown) is usually located at the $x<0$ end, near the dense reservoir, in most cases.

the table rotation period, T, $g' = (\Delta\rho/\bar{\rho})g$ is the reduced gravity at the two-layer interface and H the total depth of the water in the channel.

The primary non-dimensional parameter determining the flow properties is the Burger number

$$B_u = \frac{R}{W} \quad (1)$$

(Dalziel, 1990). In the non-rotating limit, $B_u = \infty$.

An additional parameter is the Ekman number, $\mathrm{E}k = 2\nu/fH^2$, which represents the importance of frictional effects. Here ν is the molecular kinematic viscosity, as we assume our flows to be laminar. The frictional boundary layers scale as follows:

$$\delta_{\mathrm{E}k} = \mathrm{E}k^{1/2}H \quad (2)$$

is the approximate height of the vertical Ekman boundary layer on the bottom of the channel (e.g. Tritton, 1988, p. 228) and

$$\delta_{\mathrm{S}} = \mathrm{E}k^{1/4}H, \quad (3)$$

is the approximate width of the Stewartson boundary layers adjacent to the side walls (Greenspan, 1968, pp. 30 and 97). Three other non-dimensional parameters are the aspect ratios of W/L, and H/W, and the ratio W/X of the channel width to the effective radius of the reservoirs.

2.2. Small platform

The experiments on the small platform were realized in a perspex tank (wall thickness ~1.2 cm) measuring $(H \times W \times L)$ $30 \times 56 \times 87\,\mathrm{cm}^3$, with the corresponding maximum volume of 146 l, mounted on a rotating table with diameter 1 m. The table was carefully leveled to <1 mm/m and the rotation period could be set to an accuracy of 1%. The tank is divided into two reservoirs with a connecting channel $(H \times W \times L)$ $20 \times 20 \times 29.4\,\mathrm{cm}^3$, which was fitted with curved inserts to vary smoothly over 24 cm along the channel to reduce its width by 5 cm at the narrows.

The depth of the density interface was measured by dyeing one layer, usually the lower, and recording the images using a COHU 4980 monochrome camera with a remote head, positioned to give a plan view of the channel via a mirror mounted above to maximize the path length and minimize distortion at small focal length. The flow was lit indirectly from below the channel by two sets of halogen floodlights reflecting off an angled piece of plastic-covered cardboard. The camera was directly connected to a frame grabber, acquiring images of 512×512 pixels, which is close to the actual resolution of the camera. This non-intrusive method, best suited to the small dimensions of the platform, is described in the appendix and allowed the calculation of 2-D interface depth fields within the channel accurate to 7% of the total water depth.

2.3. Large platform (Coriolis)

Two-layer rotating exchange flow experiments were also carried out on the large rotating platform at CORIOLIS/LEGI in Grenoble, France. The setup and measurement techniques are described in the following sections and Appendix B.

2.3.1. Setup

The 13 m diameter tank, mounted on the 14 m diameter rotating platform, was modified to form two reservoirs connected by a flat-bottomed, horizontally contracting channel. A plan-view sketch of the setup is given in Fig. 2 and a photograph is shown in Fig. 3. The platform rotation period could be set with an accuracy of 10^{-2} s. Measurements were made from plan-view

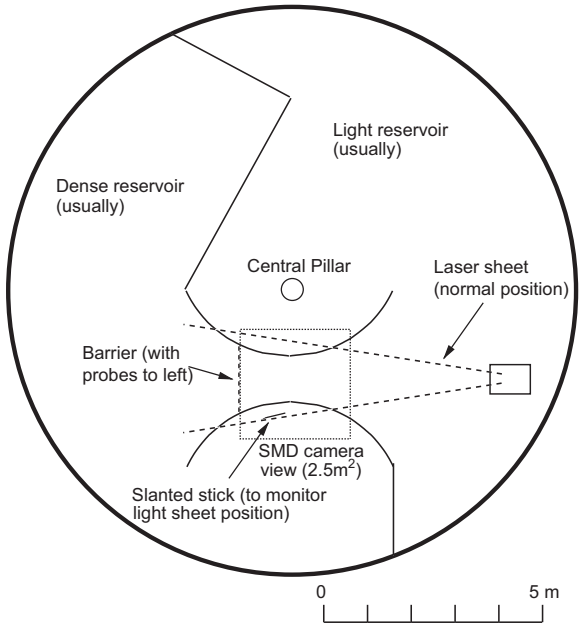

Fig. 2. Plan view schematic of setup in the *Coriolis* rotating tank. The camera field of view is centered in an across-channel direction and offset slightly from the channel center toward the laser. The barrier is located just to the left of this field. Note the field of view varied slightly with depth due to parallax.

Fig. 3. Elevated view of the setup in the *Coriolis* rotating tank. The scanning laser head and mirror were fitted inside the gray box fixed to the tank rim with a steel bar. The observation bridge held the actual laser (connected to the laser head below) and computer acquisition equipment, connected to the camera located above the center of the channel below. The channel connected the two large reservoirs and had a removable barrier.

images of particles suspended in the water, illuminated by a laser. Therefore, all walls were made of perspex sheets, reinforced with wood, to allow passage of the laser light; however, absorption of the laser light by the perspex was found to be too great to allow sufficient illumination of particles near the side walls at the barrier end. The removable barrier, initially separating the two fluids, was located just outside the field of view of the camera.

The digital camera, an SMD/DALSA 1M60 with a $14 \times 14\,\mathrm{mm}^2$ CCD chip providing 12 bit digital output at a resolution of 1024×1024 pixels, was fitted with a 25 mm Schneider lens and mounted near the channel center 4.3 m above the standard water surface, which was 0.60 m above the bottom. This gave a view of a large part of the channel while retaining sufficient resolution to observe important features in the flow.

The laser was located outside the channel opposite the barrier and set to illuminate a sequence of horizontal slices between 6 and 54 cm above the bottom. The horizontal scan of the laser was synchronized to the SMD camera, set to allow acquisition of frames at up to 30 Hz, and illuminated most of the SMD field of view. The laser was set to consecutively scan up to nine discrete horizontal levels in most experiments. All nine levels could be scanned in approximately 15 s. The laser sheet was 4 mm thick in the first experiments but later set to 10 mm, as this was found to reduce the effect of particles moving vertically in and out of the light sheet, which can lead to false velocity values in the image processing technique outlined in Appendix B.

To avoid wind-induced motion, plastic sheets, covering approximately half of the reservoir surfaces, were used for most experiments. Uniform reservoir densities were achieved using two electric mixers with a volume throughput of $20\,\mathrm{m}^3/\mathrm{h}$, operating near the tank rim before and after each experiment. This allowed mixing of the reservoirs, each holding approximately $40\,\mathrm{m}^3$, within 2–3 h. Our intended density difference was $10^{-3}\,\mathrm{g\,cm}^{-3}$ but in practice this value varied by up to $\pm 20\%$ between experiments.

Particles (Pliolite DF01) with diameter 0.1–0.2 mm were added to the water and resuspended by sweeping the reservoir floors prior to spinning up each experiment. Images of these particles are used to infer velocity using the correlation imaging velocimetry (CIV) method, as described in Appendix B. This method allowed the calculation of 2-D horizontal velocity fields with an accuracy of $0.12\,\mathrm{cm\,s}^{-1}$ at the different laser levels described above.

2.3.2. Interface depth

The CIV velocity fields were used to infer the depth of the interface by vertically interpolating the horizontal velocity at each horizontal grid point using a piecewise cubic hermite interpolant (Matlab implementation; for algorithm see Fritsch and Carlson, 1980; Kahaner et al., 1988). This was found to give the best representation of a two-layer profile while keeping edge effects near the surface and channel bottom to a minimum.

The interpolated profiles were found to give a good indication of the 'shear' interface by locating the depth of the zero-velocity isotach, h. This process was aided by consecutive smoothing of the h fields using a 7×7 moving window median filter. The root mean square (RMS) of the difference between the filtered and unfiltered points in each window is also calculated. If the difference between the center point of the window in the input h field and the smoothed one is bigger than 4 times this RMS, the center-point of the window is marked as an outlier. Such points are repeatedly set to their original, unfiltered value and the filter is again applied. After three iterations of this process all final outliers are marked as bad. For $B_u > 1$, the h fields could be successfully calculated, but at higher rotation multiple velocity minima in the water column and stagnant regions create too much noise in the h fields.

At the narrows the zero isotach is expected to be similar to the density interface measured on the small platform, but may deviate toward the

reservoirs because of entrainment into the thinner layer (Hogg et al., 2001; Stenström, 2003).

2.4. Density and fluxes

The time-mean exchange flux over the whole of a lock-exchange experiment can be calculated from density measurements of the (well-mixed) reservoirs before the barrier is removed and after it has been replaced. This procedure was used on both platforms.

The dimensional exchange flux is given by

$$\bar{q^*} = \frac{|\Delta\rho_m| V}{t\Delta\rho}, \tag{4}$$

where V_m is the volume and $|\Delta\rho_m|$ the difference in initial and final density of reservoir m. The initial density difference between reservoirs 1 and 2 is $\Delta\rho$, and t is time between opening the barrier and closing it again (Whitehead et al., 1974). This only requires three measurements of ρ, as the final ρ is only required for reservoir m. Using both $m = (1, 2)$ gives two different values of $\bar{q^*}$ that should be equal, the difference is thus a measure of the experimental error.

Density was measured on the small platform using either an Autosal salinometer together with a digital thermometer, accurate to $2.3 \times 10^{-5}\,\mathrm{g\,cm^{-3}}$, or a hydrometer with accuracy $5 \times 10^{-4}\,\mathrm{g\,cm^{-3}}$. On the *Coriolis* platform a hydrometer accurate to $10^{-4}\,\mathrm{g\,cm^{-3}}$ was used. On the large platform it was also possible to estimate the instantaneous fluxes by integrating the product of the measured velocities and layer depths across the channel.

3. Results and analysis

In this section we consider first whether or not the flow is steady before discussing in greater detail the behavior for different Burger numbers, the fluxes and whether or not the flow is hydraulically controlled. A list of the experiments presented in this paper is given in Table 1. There are a total of 15 experiments on the small platform and three experiments on the *Coriolis* platform. To further verify the method to determine the quasi-steady states in our experiments and understand the role of friction and initial conditions, simulations of the experiments were made with a two-layer isopycnic coordinate model (MICOM). Details of the model are given in Appendix C. In the model the reservoirs are square in plane form but otherwise the geometry is the same as in the experiments.

Table 1
List of experiments for the *Coriolis* platform (gray background) and the small platform

B_u	T (s)	H (cm)	W (cm)	g' (cm s^{-2})	Volume flux (dm^{3}s^{-1})	Running time (s)
0.90	150.00	60.0	102	0.98	4.6	1720
4.16	750.00	60.0	102	0.83	7.2	2780
0.21	30.00	59.4	102	1.37	1.6	5460
0.34	5.24	14.5	8.8	3.7	0.04	228
0.49	7.85	14.5	8.8	−3.3	0.05	171
0.51	7.85	14.5	8.8	3.4	0.05	171
0.6	7.85	14.5	8.8	5.9	N/A	101
0.55	7.85	14.5	8.8	4.1	0.17	171
0.62	9.67	14.5	8.8	3.4	0.07	124
0.87	14.96	14.5	8.8	2.9	0.11	81
1.1	18.48	14.5	8.8	3	0.02	64
1.4	22.05	14.5	8.8	3.6	0.49	61
1.6	26.18	14.5	8.8	3.3	0.13	65
1.8	29.92	14.5	8.8	3.1	0.21	60
1.8	38.08	14.5	8.8	2	0.12	60
1.9	33.07	14.5	8.8	2.8	0.15	61
2	36.96	14.5	8.8	2.5	0.14	51
2.5	40.54	14.5	8.8	3	0.11	60

The flux measurements are calculated from the change in reservoir density and the running time. Note that in experiment 711 density was measured with a hydrometer with an error of $5 \times 10^{-4}\,\mathrm{g\,cm^{-3}}$, i.e. one order of magnitude higher than the other experiments on the small platform. In the experiment with $B_u = 0.49$ the reservoir densities were reversed relative to the other experiments.

3.1. Timescales and variability

The primary interest of this study is the quasi-steady state of a rotating, two-layer exchange flow, but selecting this state from the data in each experiment requires a look at the transient behavior. The evolution of each lock-exchange experiment can be considered in three stages: the initial adjustment and concurrent establishment of the exchange flow, the (quasi-)steady exchange during which the changing reservoir conditions do not affect the exchange flow and finally the communication of changes in reservoir conditions to the strait via gravity currents and waves. A convenient way to identify these stages is by looking at a time series of properties at the narrows.

In the *Coriolis* experiments, the instantaneous exchange fluxes, computed from the velocity field, are a useful indicator of the flow state. In Fig. 4 the non-dimensionalized flux

$$\bar{q} = \frac{\bar{q^*}}{g'^{1/2} H^{3/2} W}, \tag{5}$$

is shown for $B_u \sim 4$. After the barrier is lifted there is a sharp increase in exchange flux during the adjustment phase. This is followed by a period of approximately steady flux, indicating an insensitivity to the gradual change of conditions within the reservoirs. However, eventually the reservoir conditions start to influence the channel, leading to a slow decrease in the flux toward the end of the experiment. The onset of this event is triggered by gravity currents from the initial transients, that circumnavigated each reservoirs and again intrude into the channel. Analysis of the MICOM simulations, where again $\bar{q}$ could be calculated, revealed a similar sequence of events.

On the small platform, the mean interface depth on the RHS is used to determine the state of the flow in a similar way to the flux measurements. Here, the assumption is made that a steady hydraulically controlled exchange is associated with an approximately constant flux and interface depth across the narrows, although the transient phases are likely to show up differently in the flux and interface depth records. Thus, the time series are used primarily to look for the steady parts and not to compare the transient behavior between those experiments with only velocity and those with only interface depth measurements. For each experiment these time series were used to identify a period during the steady or quasi-steady stage that was then used for the analyses presented in the following sections.

In contrast with the linear adjustment of a dam-break flow in a rotating channel, first examined by Gill (1976), the depth changes across the barrier are comparable with, indeed the same as, the total depth of the fluid. Hence, non-linear advection is important (e.g. Helfrich et al., 1999; Hermann et al., 1989), and the presence of the side walls gives the adjustment process the character of a gravity current. The timescale for the initial adjustment is of the order of f^{-1}, which is seen in the onset of flux

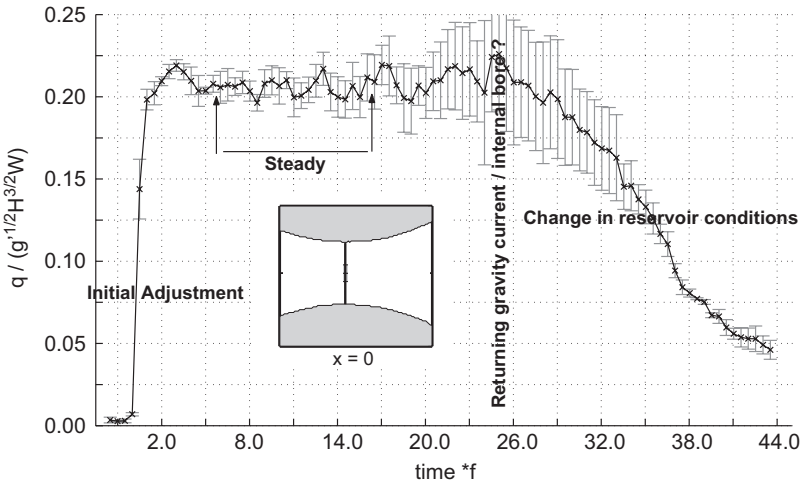

Fig. 4. Time series of non-dimensional exchange flux at the narrows $\bar{q}$ for $B_u \sim 4$. The difference between the measured absolute flux in the upper and lower layers is shown as error bars. Note the different stages of the experiment: the initial adjustment, the steady phase, a returning gravity current or bore and the change in reservoir conditions near the end.

at the narrows for $t>1$, for example in Fig. 4. Only for $B_u \ll 1$ do we expect this to be longer due to a significantly reduced flux in the rotationally limited gravity current, but we were not able to distinguish the end of this adjustment as the flow did not reach a steady state but continued to be transient in nature throughout.

Once the gravity currents have passed through the channel into the downstream reservoirs they will begin to alter the conditions there. If the flow is hydraulically controlled, a region of supercritical flow will be established between the control section and the two reservoirs, isolating the control section from these changes (i.e. small amplitude long waves are only able to propagate away from the control section). The details of this process of establishing a steady flow are not yet clear and cannot be determined from our data, but the time to establish the quasi-steady exchange was found from the time series to be of the order of several inertial periods (f^{-1}), which is significantly longer than the time needed for the initial adjustment alone. In non-rotating flows the control will eventually be flooded and the exchange altered if there is a sufficient change in the downstream reservoir (Dalziel, 1991). In our rotating experiments the first changes appear to occur once the gravity currents have circumnavigated the reservoirs and returned to the channel. The expected travel time of the gravity current around the reservoirs is given by

$$T_r = (2+\pi)\frac{X}{a(g'H)^{1/2}}, \tag{6}$$

where X is the tank radius. Studies of rotating gravity currents (e.g. Griffiths and Hopfinger, 1983) suggest that the constant a is of the order of $(h/H)^{1/2}$, where h is the depth of the current upstream of the bore. The depth of the current was not observed, but the return time of the gravity current suggested a was 0.1–0.3, which is broadly consistent with the suggested scaling.

In the laboratory we have, in addition to the time scales above, the spin-up time. The selected (quasi-steady) periods were chosen to start at least one spin-up time period from the beginning of the experiment, to ensure the boundary layers were fully developed. However, when rotation was weak the spin-up time was long so that this was not possible due to the finite volume of the reservoirs, for example in the $B_u \sim 4$ experiment.

Similar time series to the one in Fig. 4 were observed for most $B_u \geqslant 1$, on both platforms and in the MICOM simulations, although not all laboratory experiments were run long enough to see the final stage. For $B_u<1$, the flows were found to be unsteady, but it was possible to identify several quasi-steady periods in many cases. For $B_u \ll 1$, however, the flow was found to be always unsteady and flux records, where available generally showed oscillations of similar amplitude as the mean flux, mainly due to a meandering current and vortices propagating through the narrows cross-section. This time-variability analysis was then used to determine a value for the time mean flux, $\bar{q}$, for one or more quasi-steady time periods or instantaneous times, as appropriate. The following sections describe the (quasi-)steady velocity and interface depth fields, first for $B_u \geqslant 1$ and then the variable flow for $B_u<1$.

3.2. *Flow with* $B_u \geqslant 1$

A three-dimensional representation of the channel volume is shown in Fig. 5a, where velocity vectors as well as speed are given on different horizontal and vertical slices. This experiment, performed on the *Coriolis* platform with slow rotation, $B_u \sim 4$, shows fairly straight flow, in particular at the narrows. The lower layer is coming from the dense reservoir (negative x), thinning toward the light reservoir and vice versa for the light, upper layer. Velocity at the narrows is almost equal and opposite in both layers. This is similar to non-rotating flows. Unlike the latter, however, there is a small slope of the interface across the channel. There is also a noticeable cross-channel variability in speed. In particular, as the dense layer exits the channel, the speed on the left side becomes very small suggesting that it separates from the left-hand wall just outside the field of view. This layer separation is also evident in the depth of the zero-velocity isotach in Fig. 6a that is close to the channel floor near the light reservoir. We expect a separation for the upper layer to occur in a similar manner close to the dense reservoir, although this region is outside the measurement domain.

As B_u decreases the cross-channel interface slope increases. For $B_u \sim 1$ (*Coriolis* platform, Fig. 5b; small platform, Fig. 6b and c) the flow separates closer to the narrows. In the experiments on the small table there is an apparent asymmetry between the upper and lower layers with the lower layer being a little thicker than the upper layer. This is particularly evident in Fig. 7a which shows the

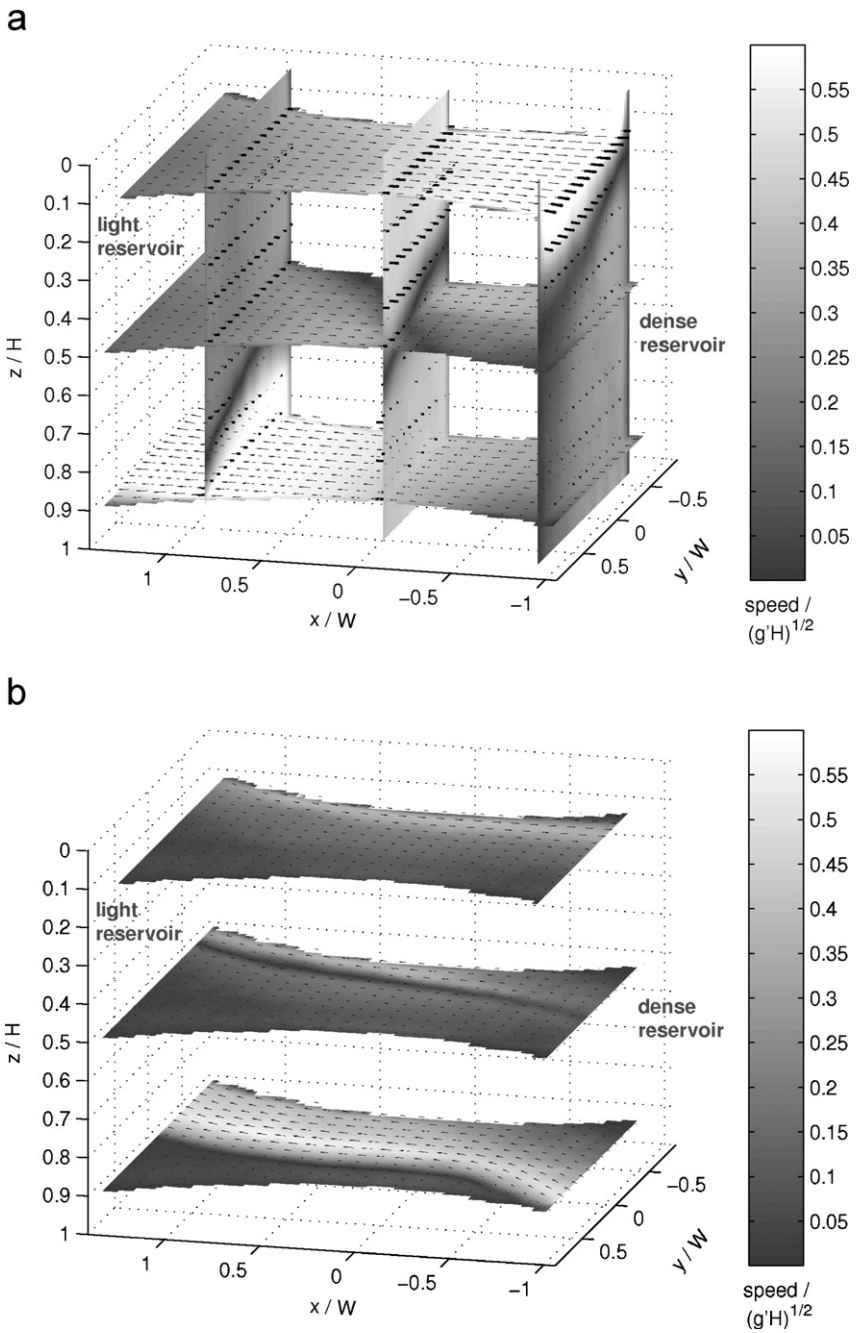

Fig. 5. Quasi-steady time average of the horizontal velocity and speed in the channel for (a) $B_u = 4$, and (b) $B_u = 0.9$. The interface is represented by the zero-velocity isotach (black shading). Note that in (b) only three levels were observed and it was not possible to interpolate onto the vertical planes as was done in (a) with nine vertical levels.

interface height across the control section for a range of B_u. This is most likely due to the effects of bottom friction. Zaremba et al. (2003) showed for non-rotating flows that bottom friction leads to an increase in thickness of the lower layer. On the large platform only three levels were observed so it is not possible to determine the level of the interface accurately; nevertheless, an asymmetry is evident in

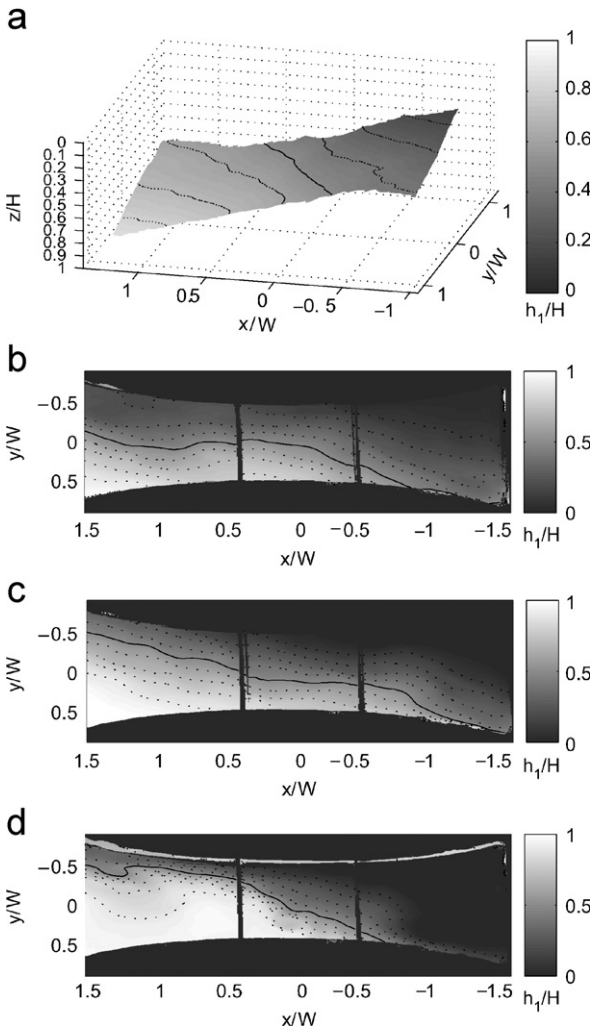

Fig. 6. Interface depth for $B_u\sim$ (a) 4, (b) 1.1, (c) 0.9 and (d) 0.3. The interface depth is represented by the zero-velocity isotach ($B_u\sim4$) and in the other cases by the density interface inferred from dye attenuation measurements. Quasi-steady time averages shown for $B_u \geqslant 0.9$ and instantaneous field for $B_u\sim0.3$. The soid line represents $h_1/H = 0.5$ and the dashed lines contour in intervals of 0.1.

the velocity fields (Fig. 5b). The lower layer crosses the channel upstream of the narrows, whereas the upper layer flow stays close to the left-hand wall as it passes through the narrows.

Theoretical results for zero-potential vorticity exchange flows by Dalziel (1990) (see Fig. 8) suggest that the cross-channel slope of the interface at the

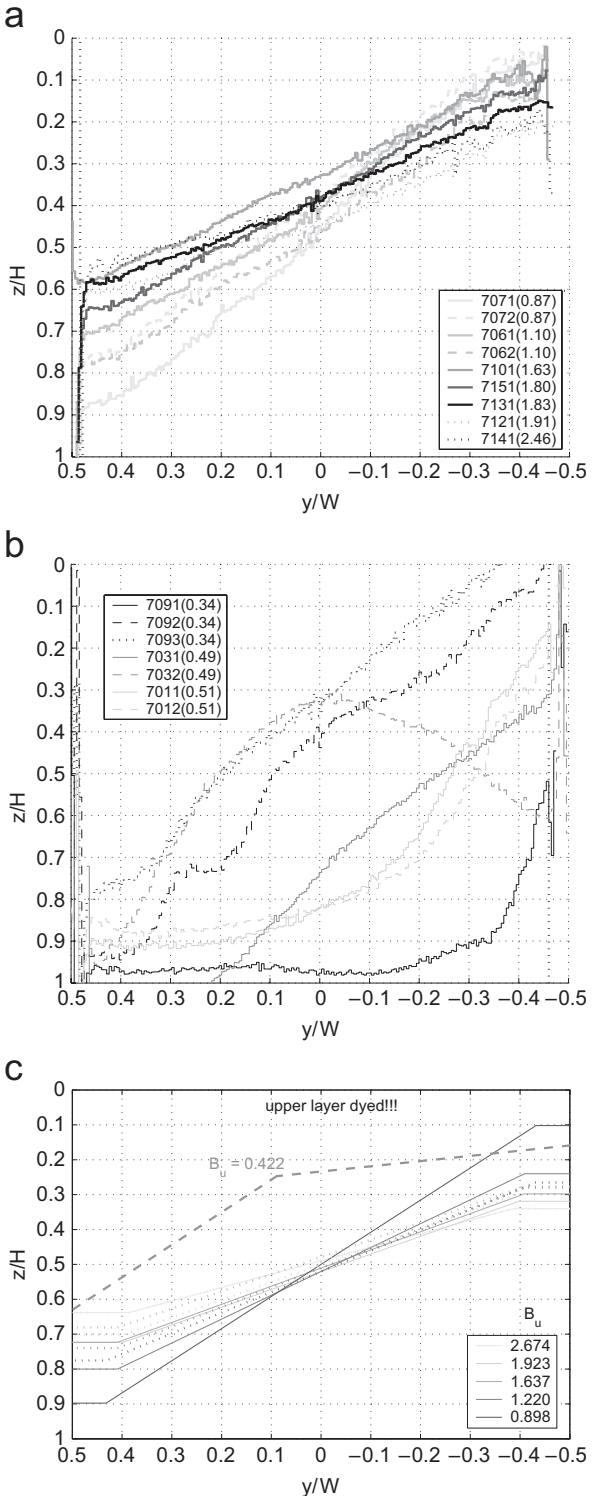

Fig. 7. Density interface depth at the narrows cross-section for (a) $B_u \geqslant 0.87$ (quasi-steady time average) and (b) $B_u \leqslant 0.51$ (instantaneous). Also shown in (c) are results from Dalziel's (1988) laboratory experiments (dotted lines, reproduced from narrows cross-sections with fluorescene dye in the upper layer) and Dalziel's (1990) semi-geostrophic theory (solid lines). The latter also includes a viscous correction incorporating the Stewartson side wall boundary layers.

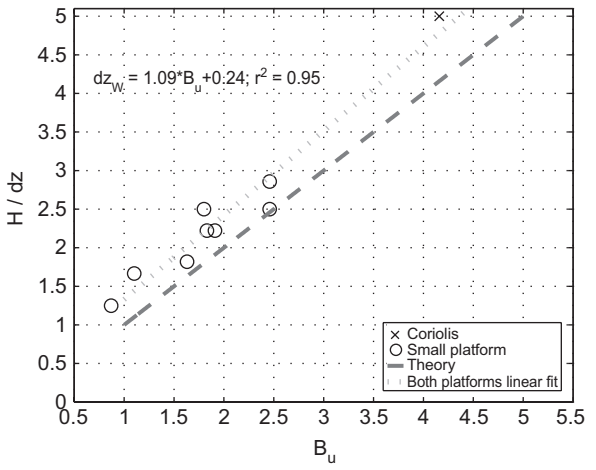

Fig. 8. The inverse of cross-channel depth change at the narrows, $H/\mathrm{d}z$, vs. B_u. Also shown is the approximate relation seven derived from inviscid zero-potential vorticity theory.

narrows is inversely proportional to the Burger number, such that

$$\frac{\mathrm{d}z}{H} \approx \frac{W}{R} = \frac{1}{B_u}, \tag{7}$$

where $\mathrm{d}z$ is the dimensional difference in interface height between the two side walls at the narrows and H the dimensional channel depth. A similar relationship is found in our experiments (see Fig. 8). The observed values of $\mathrm{d}z$ were taken from the cross-sections in Fig. 7a and the values at the $x = 0$ section in Fig. 6a. The agreement is remarkably good considering the assumptions of zero-potential vorticity and inviscid flow in the theory. Both finite potential vorticity and viscous effects are expected to reduce $\mathrm{d}z$ (Dalziel, 1990) as is observed in Fig. 8. Note that our setups have finite depth reservoirs and therefore, in each of the setups, the reservoirs will initially have the same finite value of potential vorticity.

Eq. (7) suggests that for $B_u > 1$ the interface will be attached to both side walls at the narrows, but for smaller Burger numbers the interface will separate from the sides. Our results on the small platform suggest that the flow is close to separating for $B_u = 0.9$; however, even for much smaller Burger numbers complete interface separation at the narrow was rarely observed, as seen in the density interface cross-sections from the small platform (Fig. 7b) and similar observations from experiments by Dalziel (1988), as shown in Fig. 7c. This lack of separation is perhaps due to the frictional effects in the bottom boundary layer.

3.3. Flow with $B_u < 1$

As B_u decreases below 1 the relative magnitude of unsteadiness increases, and flows with $B_u \ll 1$ are dramatically different from those with $B_u \geqslant 1$. At small Burger numbers, vortices and meanders propagate through the channel so that the flow is always unsteady and the magnitude of the variations in the exchange are of the same order as the mean flux. Two snapshots of an experiment with $B_u = 0.2$ are shown in Fig. 9. The width of the currents is small, typically of the order of the Rossby radius, which agrees with existing theory (e.g. Pratt and Armi, 1990; Dalziel, 1990). When channel crossing was observed the current crossed the channel within a downstream distance of the order of $3R$. The crossing meant that the baroclinic part of the exchange flow in each layer was only close to a wall for some parts of the channel and, where fully separated, represented a frontal flow.

The steep interface slopes and recirculating flow within the meanders and vortices in this regime make it very difficult to determine the interface between the two layers from velocity measurements alone. However, a better picture of the interface depth was obtained in the experiments on the small rotating table (e.g. as shown in Fig. 6d). Whilst the interface position was highly variable, on average the lower layer was thinner than the upper layer (see also Fig. 7b). This is the opposite to flows with $B_u \geqslant 1$ where, as in non-rotating flows, bottom friction led to the lower layer being deeper. The reasons for these differences are examined in the discussion where the laboratory results are compared with numerical simulations.

3.4. Exchange fluxes at the narrows

Whitehead et al. (1974) used semi-geostrophic, zero-potential vorticity theory to derive an estimate of the expected maximal flux in the exchange flows over sills. The estimated flux, non-dimensionalized as in Eq. (5), is given by

$$\bar{q} = \bar{q}_{\mathrm{whitehead}} = \begin{cases} \dfrac{1}{4}\left(1 - \dfrac{1}{3}\dfrac{1}{B_u^2}\right) & \text{for } B_u > 1, \\ \dfrac{1}{6}B_u & \text{for } B_u < 1. \end{cases} \tag{8}$$

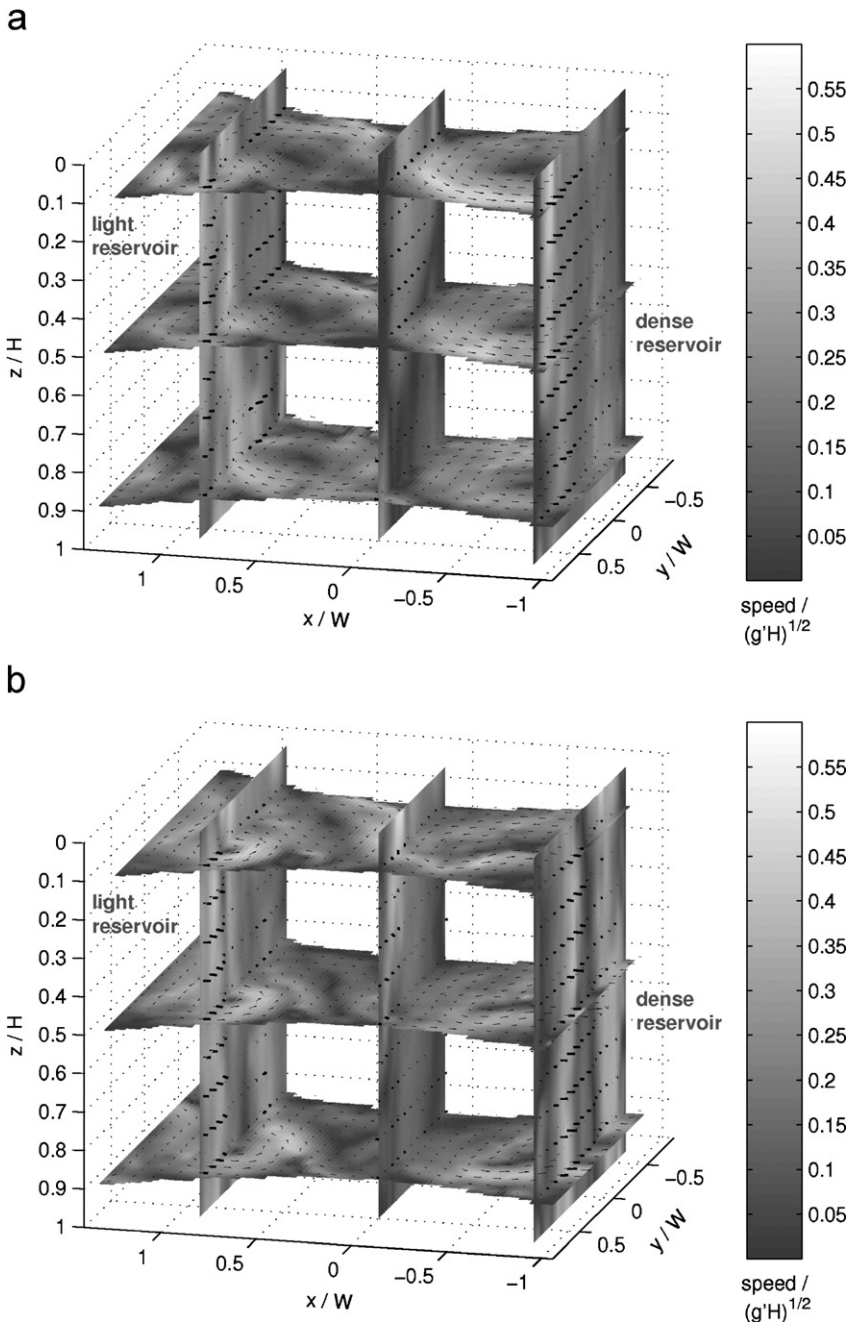

Fig. 9. Instantaneous horizontal velocity and speed in the channel center for $B_u \sim 0.2$ at times $t =$ (a) $597f^{-1}$ and (b) $479f^{-1}$. Note the flow shows significant vortices and a channel crossing of the currents in the vicinity of the narrows.

As $B_u \to \infty$, $\bar{q}$ approaches $\frac{1}{4}$, which is the non-rotating maximal flux. Dalziel (1990) and Riemenschneider et al. (2005) have derived results similar to Eq. (8) from more complex theories. The theoretical $\bar{q}$ is given as a solid line in Fig. 10. The measurements on both platforms from density measurements give an estimate over one whole experiment. These are shown as well as similar measurements by Dalziel (1988). On the *Coriolis* platform the CIV velocities during the quasi-steady period, or at selected points in time for $B_u \ll 1$, give an additional estimate of $\bar{q}$. Exchange fluxes derived

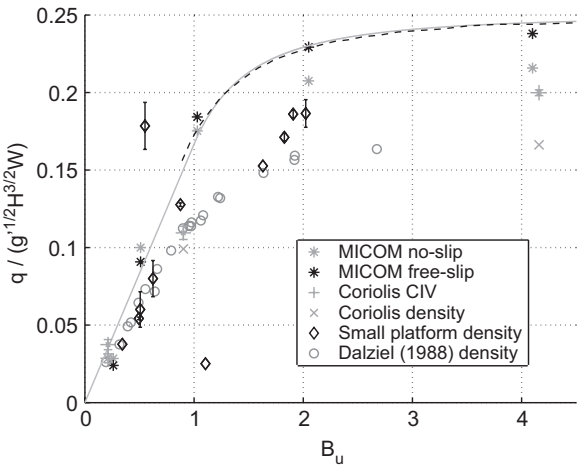

Fig. 10. Time-averaged non-dimensional exchange fluxes ($\bar{q}$) vs. B_u. On the *Coriolis* platform, velocity (CIV)-based estimates were available. Other estimates are from density measurements of the reservoirs before and after the experiments from both platforms. Results from Dalziel (1988) are also shown. Fluxes from density measurements without error bars are hydrometer-based estimates with an error ~50% (small platform) and ~10% (*Coriolis*) of $\bar{q}$, otherwise error bars are as shown. In addition, fluxes from the MICOM simulations with a no-slip and free-slip condition at the side walls are shown. The lines represent the theoretical prediction of Whitehead et al. (1974) given in Eq. (8) (solid line) and our own theoretical solution for finite potential vorticity (dashed line; this solution becomes invalid for $B_u < 0.87$).

from the velocity fields in the MICOM simulations are also shown.

The density-based estimates are generally lower than the velocity-based ones, as the whole experiment includes the unsteady time periods, i.e. the initial adjustment and in some cases the final stage in which the change in reservoir conditions influences the channel interior. Fluxes are found to vary with B_u in a similar manner as the inviscid zero-potential vorticity prediction but are overall lower. In our flows, potential vorticity is expected to be finite, as the channel is the same depth as the reservoirs. To estimate the effect of finite potential vorticity, we present a theoretical solution for constant potential vorticity in Appendix D. As in our setup, we assume depth to be uniform in the channel and the reservoirs. The solution, plotted for $B_u > 0.87$ in Fig. 10, shows a reduction of only a few percent for large B_u relative to the zero-potential vorticity theory and an increase for $B_u < 1.3$ of up to 5%. Viscous effects are likely to be more important in the reduction of the exchange fluxes, in particular for $B_u \gg 1$. At the side walls, the channel floor and the interface the flow is slowed down within the boundary layers, narrowing the effective channel width available to the inviscid exchange. This also explains the slightly higher time-mean fluxes on the small platform in comparison to Dalziel's (1988) results, as his platform was of similar size but had a rigid lid and thus an additional frictional boundary layer. At the interface, mixing and entrainment between the two layers also play a role. We shall return to this issue in the discussion in Section 4.

In contrast to the experiments, the MICOM fluxes (stars in Fig. 10) actually show a marginal increase in exchange fluxes by up to 10% for $B_u \sim 1$ and 0.5, relative to the theoretical prediction. Applying a no-slip condition on the side walls appears to increase the flux relative to the free-slip case by around 10% for $B_u \leqslant 0.5$. The only published theoretical work known to us that suggests an increase in exchange fluxes with decreasing Burger number is Timmermanns and Pratt (2005). They use theoretical arguments to link zero-potential vorticity flow over a shallow sill in a channel of constant width to the upstream conditions in adjacent reservoirs. They find that the steady exchange flux increases with rotation for $B_u < 0.64$ if the flow is detached from both walls. However, the flux prediction (their Fig. 16) increases to values much beyond what is suggested by our data and other theoretical work. In addition, Timmermanns and Pratt (2005) state that the 'stability of such solutions and the possible retarding effect of eddies is undetermined'. Our own theoretical prediction for finite potential vorticity is closest to the free-slip MICOM flux at $B_u \sim 1$, suggesting that non-zero-potential vorticity is at least partly responsible for the high MICOM fluxes. The effect of the MICOM no-slip condition is discussed in Section 4.2.1.

For $B_u \ll 1$ when, in contrast to the steady assumption in the theory, the flow is found to be unsteady at all times during our laboratory experiments and the exchange appears to occur in transient eddies and meanders passing through the strait, it is remarkable that the mean flux is very similar to the theoretical prediction.

3.5. Hydraulic control

The hydraulic state of a non-rotating inviscid two-layer fluid in a channel with a rectangular cross-

section is determined by the Froude number

$$G^2 = F_1^2 + F_2^2 = \frac{U_1^2}{g'h_1} + \frac{U_2^2}{g'h_2}, \quad (9)$$

where U_i is the velocity and h_i the thickness of layer i. Where $G^2 < 1$, long interfacial gravity waves can propagate both up and downstream, and the flow is said to be subcritical. Where $G^2 > 1$, the two interfacial gravity wave modes are forced to flow in the same direction, and the flow is said to be supercritical. Inviscid two-layer exchange flows are controlled at locations where $G^2 = 1$ (see e.g. Armi, 1986). In general, maximal exchange flows have two controls bounding a subcritical region either side of which the flow is supercritical, and hydraulic jumps connect the supercritical regions to the subcritical flow in the reservoirs (see e.g. Armi, 1986). However, for a contraction with no sill and no net flow, the two controls are predicted to be coincident at the narrowest section.

Zaremba et al. (2003) have studied the effects of friction on two-layer exchange through a contraction using numerical simulations. In agreement with previous theoretical studies (e.g. Anati et al., 1977), Zaremba et al. (2003) found that frictional effects separate the two coincident controls moving them toward the ends of the channel. Moreover, when bottom friction is greater than surface friction, asymmetry is introduced into the flow. The depth of the lower layer increases relative to the upper layer, and the extent of the supercritical region closest to the light reservoir is reduced. In a non-rotating experiment on the *Coriolis* platform we found that G^2 was indeed critical at two enclosing a sub-critical region including the narrows. We also observed a larger area of supercritical flow in the part of the channel close to the dense reservoir than in the part of the channel close to the light reservoir.

In rotating channels, the variations of depth and velocity across the width mean that simple local application of Eq. (9) does not yield an appropriate measure of Froude number as this will vary across the channel in a way that is inconsistent with the structure of the waves it is meant to characterize. Indeed a similar problem occurs in non-rotating channels with non-rectangular cross-section (Dalziel, 1992b). While the depth changes across the width of such a channel, the fluid must remain irrotational. Therefore, the fluid velocities and wave speed do not change, and a single Froude number is appropriate at each cross-section.

For rotating flows, an appropriate definition of the Froude number must take into account the structure of the Kelvin waves in addition to depth and velocity variations across the channel width. Fig. 11 demonstrates that there are order one variations in G^2 across the width of the channel, even for $B_u = 4$, and so the naive application of Eq. (9) is inadequate to determine the hydraulic state of the flow.

Building on the theoretical work of Gill (1977), various authors have developed methods to determine the hydraulic state of strait flows, both non-rotating (Dalziel, 1991; Smeed, 2000; Lane-Serff et al., 2000) and rotating (Dalziel, 1990). Recently, Pratt and Helfrich (2005) have proposed a method for single-layer rotating flows. They argue that control occurs when

$$\left|\frac{\partial M}{\partial \gamma}\right| = 0, \quad (10)$$

where M is a vector of conserved quantities, γ is a vector of variables, and $|\partial M/\partial\gamma|$ is the determinant of the matrix $\partial M/\partial\gamma$. Pratt and Helfrich (2005) use the position of streamlines and the fluid depth on the streamlines for the variables; and the fluxes and Bernoulli potential between streamlines for the conserved quantities. Here we propose an analogue of Pratt and Helfrich's condition for two-layer flows with $B_u \gg 1$. This offers a reasonable approximation to the Froude number for two-layer rotating exchange flow in a greatly simplified framework.

We choose the variables to be the mean velocities of the upper and lower layers, $\bar{U}_i, i = \{1, 2\}$, and the

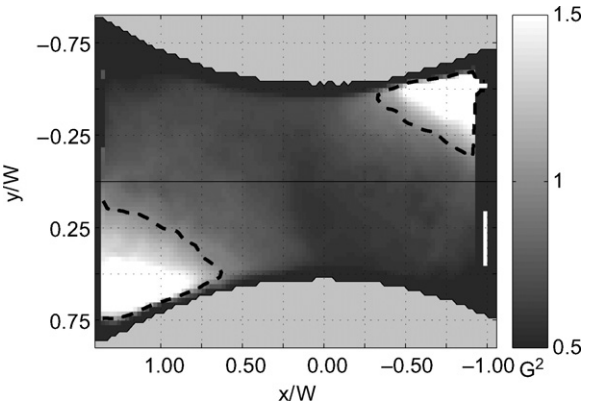

Fig. 11. Composite Froude number (G^2) field for $B_u \sim 4$. The dashed black contour represents $G^2 = 1$. Blacked-out values near the channel ends are caused by missing velocity in the upper levels due to parallax effects.

mean interface height, $\bar{h}$. The conserved quantities are the difference in Bernoulli potentials

$$\Delta B = \tfrac{1}{2}(\bar{U}_1^2 - \bar{U}_2^2) + g'\bar{h} \tag{11}$$

and the integrated fluxes in the upper and lower layers

$$q_i = \bar{U}_i \bar{h} W_s(x). \tag{12}$$

This simple set of equations is valid only in the limit of $B_u \gg 1$, when we expect the variation across the channel of the flow variables, U_i and h, to be small and linear, even if the potential vorticity is not zero. We now have three variables and three conserved quantities and

$$\frac{\partial M}{\partial \gamma} = \begin{pmatrix} \frac{\partial \Delta B}{\partial \bar{U}_1} & \frac{\partial \Delta B}{\partial \bar{U}_2} & \frac{\partial \Delta B}{\partial \bar{h}} \\ \frac{\partial \Delta q_1}{\partial \bar{U}_1} & \frac{\partial \Delta q_1}{\partial \bar{U}_2} & \frac{\partial \Delta q_1}{\partial \bar{h}} \\ \frac{\partial \Delta q_2}{\partial \bar{U}_1} & \frac{\partial \Delta q_2}{\partial \bar{U}_2} & \frac{\partial \Delta q_2}{\partial \bar{h}} \end{pmatrix}. \tag{13}$$

Substituting into Eq. (10) we find that the flow is controlled when

$$\frac{\bar{U}_1^2}{g'\bar{h}} + \frac{\bar{U}_2^2}{g'(H-\bar{h})} = 1. \tag{14}$$

This is similar to the non-rotating condition but uses a Froude number based on the variables averaged across the rotating channel. Note that if U_i and h vary linearly across the channel then Eq. (14) is equivalent to the local Froude number at the center of the channel, G^2_{y0}. This is shown in Fig. 12 for $B_u = 4$ together with the cross-channel average of the local Froude number, $\overline{G^2}$. The similarity of the two curves suggests that our approximations are indeed valid for $B_u = 4$. Timmermanns and Pratt (2005) use similar arguments with semi-geostrophic zero-potential vorticity theory. For narrow channel widths their control condition is the same as ours (their equation (31)); however, for smaller Burger numbers there are some additional terms (their equation (30)). Applying Timmermans and Pratt's equation to our velocity and interface depth data, G^2_{tp} in Fig. 12, shows that for $B_u = 4$ our approximation is very close to theirs, except near the reservoirs, where the width increases. It can be seen that the values approach unity on either side of the narrows with a sub-critical region in between, similar to the non-rotating case. It seems likely that the effects of friction keep G^2 below 1 at least at the light reservoir end of the channel. However, the approximations used to derive 14 are not valid for smaller Burger numbers. Of course, these G^2 approximations do not take into account that friction not only affects the velocities and depths, but also the wave speed so that a value of $G^2 < 1$ does not necessarily mean the flow is subcritical.

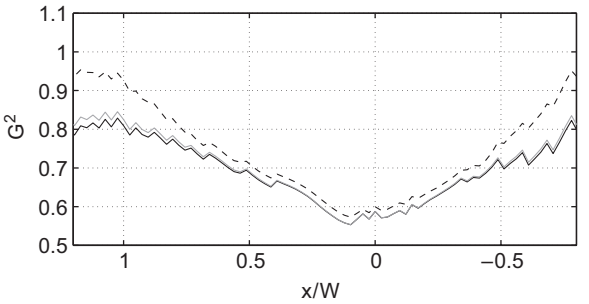

Fig. 12. Estimate of the composite Froude number along the channel, based on cross-section averaged variables (G^2_{y0}, solid line), the cross-channel mean of the G^2 fields in Fig. 11 ($\overline{G^2}$, dashed line), and after Timmermanns and Pratt (2005) (G^2_{tp}, gray line).

4. Discussion

4.1. $B_u \geqslant 1$

The results in the previous section have shown that for $B_u > 1$ the flows observed in our experiments are qualitatively and quantitatively similar to those predicted by the steady inviscid semi-geostrophic theory of Dalziel (1988, 1990) and Riemenschneider et al. (2005). Most of the differences between theory and experiment are likely due to the effects of viscosity, an issue that we need to explore in greater depth.

4.1.1. Bottom boundary layer

All experiments with $B_u \geqslant 1$ (Fig. 7a) indicate that the lower layer is relatively deeper than the upper layer. This is consistent with the friction being much greater at the bottom than the free surface, as found in numerical studies on non-rotating exchange (Zaremba et al., 2003). This conclusion is supported by the experiments of Dalziel (1988), which used a rigid boundary at the surface as well as the bottom, and the cross-sections measured at the narrows were symmetric (see Fig. 7c).

4.1.2. Side wall boundary layers

Frictional boundary layers, known as Stewartson layers, also occur on the side walls. Dalziel (1988) showed that these boundary layers effectively

reduce the channel width available to the inviscid exchange, leading to lower fluxes. The sloping interface flattens near the side walls, which is enhanced by the secondary circulation associated with the interfacial Ekman layers. This can be seen in Fig. 7c, where the flattened interface region near the side walls is comparable to the theoretical width of the Stewartson layers. In our experiments these boundary layers are apparent, (see e.g. Fig. 7a); however, it was difficult to quantify the width of these layers accurately.

4.1.3. Interfacial boundary layers and mixing

Interfacial friction and mixing is also expected to modify the exchange. Studies on non-rotating exchange, by Stenström (2003) and Hogg et al. (2001), have examined the entrainment from the thicker layers flowing towards the narrows into the thinner and faster layers leaving the strait. Such entrainment reduces the exchange flux and displaces the zero-velocity isotach towards the mid-depth near the reservoirs.

We have examined entrainment in the experiments on the *Coriolis* platform by quantifying the change in transport of each layer as a function of distance along the channel. Fig. 13 shows the change in flux relative to that measured at the narrows, as a percentage of the exchange flux at the narrows. The calculations were made in the thicker of the two layers, which contains more velocity measurements and thus provide a more accurate measure. This measure of entrainment, $(q(x)^* - q^*)/q^*$, is seen to be positive near the dense reservoir, indicating entrainment into the thinner upper layer,

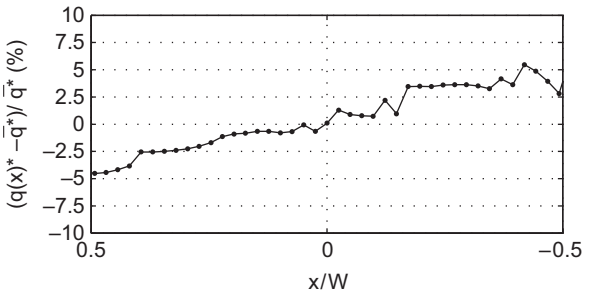

Fig. 13. Along-channel variation of the exchange flux as a percentage of the narrows exchange flux ($\bar{q}^*$) for $B_u \sim 4$. This flux, $(q(x)^* - q^*)/q^*$, was calculated in the upper layer for $x > 0$ and the lower layer for $x < 0$. Positive values represent entrainment into the upper layer while negative ones entrainment into the lower layer. Note that values $|x| > 0.5$ are not shown due to error in the thinner layer velocity profile, represented by only one measurement in the vertical close to the reservoirs.

whereas near the light reservoir fluid entrains into the lower layer. The entrainment is relatively small at around 5% of the exchange rate at the narrows and is close to the flux measurement error (~2.5%, see also Fig. 10), which indicates that entrainment is present but not very significant. Therefore, the assumption of an approximately two-layer flow is reasonable.

The low-level entrainment in this rotating experiment is significantly smaller than we found in a non-rotating experiments on the *Coriolis* platform (not shown here) where a 10% reduction in the exchange flux was observed along the channel. Nevertheless, this value is still less than estimates of entrainment effects on the flux using the theoretical arguments and empirical relationship of Hogg et al. (2001), that predict a 15% flux reduction in our setup.

Johnson and Ohlsen (1994) found in laboratory experiments that the effect of friction in reducing the exchange is lessened by rotation. They attributed this primarily to rotation limiting the size of the boundary layers at the interface and the channel sides, although the details of how interfacial friction would affect the development of turbulence at the interface and thus entrainment in our rotating experiments is beyond the scope of this paper.

4.2. $B_u \ll 1$

Flows with $B_u \ll 1$, are very different from those with $B_u \gg 1$. In particular, the flows observed in experiments with $B_u \ll 1$ are all unsteady, which agrees with the experimental results of Whitehead and Miller (1979). Variability was observed both on timescales from the order of a rotation period up to 10's of rotation periods. However, the time mean exchange flux (Fig. 10) is very similar to that predicted by the theory of Dalziel (1990) for steady flows, and is limited not by the width of the strait, but by the size of the Rossby radius.

Dalziel (1990) suggested that control of flows with $B_u \ll 1$ may occur through the channel-crossing of a separated two-layer region of the exchanging currents, where Kelvin waves are replaced by frontal waves, communicating baroclinic information on the interface. The application of these ideas to the unsteady flows described here is however, unclear. An alternative view of hydraulic control that encompasses unsteady flows has been presented by Stern (2004), who suggested that the controlled flows are those that maximize the flux of the time

mean flow. However, Stern (2004) only considered single-layer reduced gravity flows and this approach has not yet been applied to exchange flows.

Unsteady waves and meanders have been observed in wide oceanic straits, such as the Denmark Strait (Fristedt et al., 1999; Käse et al., 2003). In the case of the Denmark Strait the vortices are observed downstream of the sill, and it has been suggested that they are the result of topographic stretching of the overflow waters, a feature not present in our experiments. However, other studies have suggested that they may be the result of baroclinic (Smith, 1976) or barotropic (Fristedt et al., 1999) instabilities. Either of these instabilities could occur in our experiments.

4.2.1. Friction and time-dependence

To investigate the influence of friction on the steadiness of the exchange we turn to the MICOM simulations of our experiments. The qualitative features of the simulations were very similar to those of the experiments. In the MICOM simulations with and without the no-slip boundary condition a persistent channel-crossing during the quasi-steady states was evident for $B_u = 0.5$. For $B_u = 0.25$, however, the flow in the channel was unsteady, and eddying and meandering was apparent (see Fig. 14). However, the location of the channel crossing showed less variability than in the laboratory experiments and the flow was significantly more stable when the no-slip boundary condition (see Appendix C) was applied on the side walls. Toward the end of the no-slip run a quasi-steady flux was observed, which suggests that boundary friction does have a significant effect on the development of instabilities and eddies, in particular in the regions between separated currents and the side walls.

4.2.2. Vertical asymmetry, friction and initial conditions

In Section 3.3 it was noted that, in contrast to flows with $B_u > 1$, the lower layer was thinner than the upper layer at the narrows. There are two possible explanations for this asymmetry. First, it could be the result of friction in the lower layer, or, second, it could be the result of the position of the lock gate. To investigate this asymmetry further additional MICOM simulations were performed for low Burger number.

In Fig. 15 the depth of the interface at the narrows is shown as a function of time for several

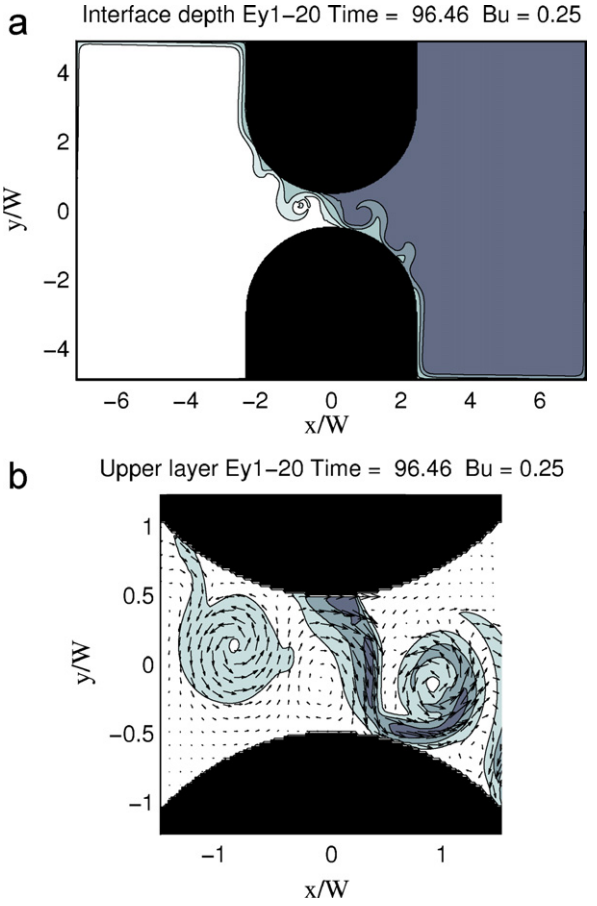

Fig. 14. Numerical simulation with $B_u = 0.25$ and $E_N \sim 0.0005$ at time $96f^{-1}$. The "barrier" was located at $x/W = 0$. (a) The depth of the lower layer h_2/H over the entire domain. The contour interval is 0.2 and the darkest shading indicates $h_2/H > 0.8$. (b) The velocity (arrows) and speed (contours) in the upper layer in the region of the narrows. The contour interval is $0.2\sqrt{g'H}$.

simulations with $B_u = 0.25$. The "barrier" initially separating the two reservoirs was displaced toward the deep reservoir in (a) and (b). In (a) there was no bottom drag and a free-slip condition was applied on the side walls. Initially there is an asymmetry with the lower layer occupying most of cross-section, however, as the flow develops the asymmetry is reduced and when $tf \sim 150$ there are approximately equal amounts of upper and lower layer fluid at the narrows. In case (b) bottom friction is applied with an equivalent Ekman number $E_N \sim 5^{-4}$. In this case we see that the initial asymmetry appears to persist. A similar result was found when there was no bottom drag but a no-slip boundary condition was applied on the side walls. Furthermore, when drag was increased by a factor

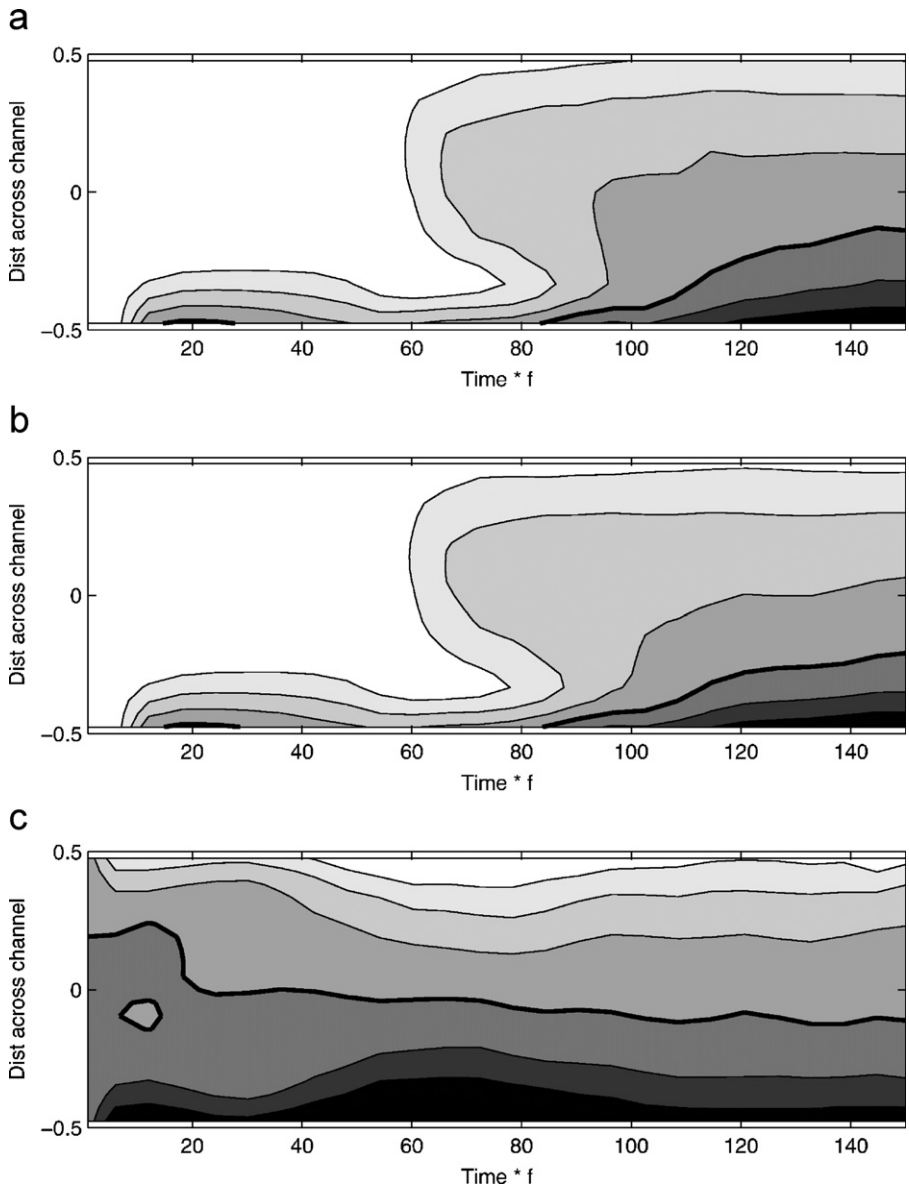

Fig. 15. The depth of the lower layer at the narrows as a function of time (non-dimensionalized by f^{-1}) for three simulations with $B_u = 0.25$. The contour interval is $0.125H$, and the thick line indicates the contour $0.5H$. In (a) and (b) the "barrier" is located at $x/W = 1.2$; in (c) it is located at $x/W = 0$. In (a) there is no bottom friction; in (b) and (c) there is bottom friction with an equivalent Ekman number $E_N \sim 0.0005$.

10 this effect was much more pronounced. In (c) the "barrier" was in the middle of the channel and bottom drag was applied in the lower layer with Ekman number $E_N \sim 5 \times 10^{-4}$. A small asymmetry develops in this case; however, it is much less than in case (b).

From the results of the numerical simulations it seems that both friction and the asymmetry in the initial conditions contribute to the asymmetry observed in the simulations. In particular, when either bottom drag or a no-slip side wall condition is applied the resulting flow pattern appears to be dependent on the initial conditions.

5. Conclusions

The primary parameter determining the transport and other features of two-layer stratified rotating

exchange flows is the Burger number, $B_u = R/W$, where W is the channel width and the Rossby radius $R = \sqrt{g'H}/f$. We have examined flows over a range of Burger numbers from ~0.25 to ~4 with the primary focus to determine the (quasi-)steady features of the exchange. The use of the CIV technique has enabled us to obtain for the first time detailed measurements of the velocity field in these flows.

The exchange fluxes measured in our experiments are in close agreement with the theoretical predictions of Dalziel (1990) and Whitehead et al. (1974) for zero-potential vorticity flow and our calculations for finite potential vorticity in Appendix D. For $B_u > 1$ the exchange flux is similar to that in non-rotating flow and increases in proportion to the width of the channel. For $B_u < 1$ the exchange flux is limited not by the width of the channel but by the Rossby radius. The characteristics of the flow are also very different for small and large Burger numbers.

For $B_u \geqslant 1$ the flow is mostly steady, and, although there is some cross-channel variation, neither layer separates from the side walls at the narrows. The distribution of the Froude number suggests that the flow is hydraulically controlled in a manner similar to that of non-rotating flows under the influence of bottom drag.

For $B_u < \approx 0.5$ the flow is very different. In particular, the flow is unsteady and meanders and eddies are observed in the strait. It is perhaps surprising that the time averaged exchange flux is in reasonable agreement with the steady-state theory. The qualitative features of these experiments agreed with a series of numerical simulations. Analysis of the laboratory experiments and the numerical simulations suggests that when either bottom drag or side wall friction is present the exchange is less time-dependent and the flux may actually be increased relative to the inviscid case. Furthermore, it is indicated that with boundary friction some features of the flow, such as the location where channel crossing occurs, may be sensitive to the initial conditions.

Acknowledgments

Thanks to the team at Coriolis/LEGI, without whom these experiments and the data processing and evaluation would not have been possible, and Harry Bryden for valuable discussions. Ulrike Riemenschneider helped set up the numerical simulations. Access to the experimental facility of Coriolis/LEGI was supported by the European Commission, Enhancing Access to Research Infrastructures action of the Improving Human Potential program of FP5, under contract HPRI-1999-CT-0006. This work was supported by the UK Natural Environmental Research Council.

Appendix A. Interface depth

The small platform setup used plan images of the channel with the (usually) lower layer dyed to infer the position of the density interface between the two layers. The frame grabber was controlled using

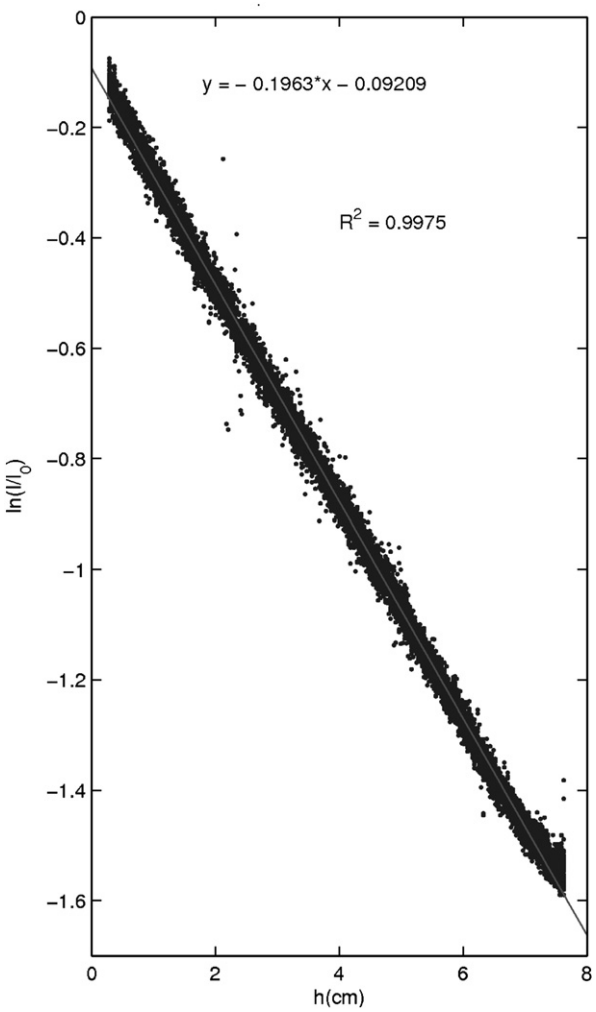

Fig. 16. Direct calibration of h vs. $\ln(I/I_0)$ at constant dye concentration $c_p = 0.07$ ml/l, using a vertically slanting container with a uniformly dyed fluid (ρ of similar magnitude as in the experiments). This gives a horizontal variation in h by geometric considerations.

DigImage V1.5 (Dalziel, 1992a), which allowed camera images to be acquired at user-specified times. Subsequent processing was done using Matlab V.6 by The MathWorks Inc. The camera system used a color filter (green, Hoya X1) and was calibrated to measure absolute light intensity. Red food coloring was used as dye in the dense fluid to visualize the interface between the two layers. The lower layer thickness, h, could be estimated using methods described in Cenedese and Dalziel (1998) and Holford and Dalziel (1996). A direct calibration of h was performed using a slanting container with a uniformly dyed fluid of horizontally varying depth. Assuming an exponential attenuation of the light passing through the fluid from the channel bottom leads to the following relationship:

$$h = \frac{-1}{Ac_p} \ln\left(\frac{I}{I_0}\right), \tag{15}$$

where $c_p = 0.039\,\mathrm{ml/l}$ is the dye concentration, A a constant of calibration, I the intensity past the fluid and I_0 the incident (background) intensity. This effectively gave a value for $-1/Ac_p$ from the calibration curve shown in Fig. 16 and allows h to be accurately measured to within 7% of channel depth. Parallax was ignored as it was found to be within the measurement error when recording a uniform dye field.

Potential shortcomings of the method are mixing of the two fluids causing a diffuse interface and filling up of regions in the initial, unsteady phase that are stagnant and/or isolated during the steady exchange, thus giving a false impression of the active part of the flow.

Appendix B. CIV

Horizontal velocity fields were inferred from consecutive camera images at the same vertical level using the CIV technique (Fincham and Spedding, 1997; Fincham and Delerce, 2000), which has previously been used on the *Coriolis* platform (e.g. Serra et al., 2002). Here we will concentrate mainly on the specific problems and solutions encountered when applying this technique to images from a two-layer exchange flow.

The images were acquired using CIVIT V.3, available from Fincham and Spedding, and the median (background) of sets of 20 images was removed to better visualize particle movement in regions of laser light reflection, bottom particle deposits and badly illuminated regions. The CIV processing was done using software developed at *Coriolis*/LEGI. Further Matlab scripts were used to correct for parallax and the refraction at the surface. The influence on parallax by the density interface between the exchanging layers and the associated refractive index change was small as the interface is expected to be at an angle of 45° or less to the horizontal for most of the flows under study. At the edge of the field of view this effect would at maximum give an error in grid position of 0.5 cm relative to the channel center; however, as adjacent pixels have a similar error, the overall effect on the local velocity calculation is negligible. The vertical deviation of the light sheet due to refraction at the two-layer density interface was found to be below 2 cm, which is only 3% of the total depth and only $\frac{1}{3}$ of the distance between laser sheet levels. Therefore, errors in the in-plane velocity measurements are not significantly affected. Erroneous velocity due to vertical particle movement in the homogeneous density layers was largely avoided by thickening the laser sheet to 1 cm together with a short-time period between the acquisition of CIV particle images. The velocity measurements were further improved by a hierarchical algorithm (Fincham and Delerce, 2000), which utilizes multiple CIV passes and intermittent smoothing to eliminate false vectors. Our setup and parameters were chosen to capture the exchange fluxes and flow field variability on the space and time scales of the two-layer exchanges under study while averaging over the smaller scales, such as shear near the interface. The CIV processing allowed the calculation of horizontal velocity accurate to $\sim 0.12\,\mathrm{cm\,s^{-1}}$ (0.1 pixels displacement) in our experiments.

Appendix C. Numerical simulations

The numerical simulations described in this paper were undertaken with the MICOM (Bleck and Boudra, 1986, 1990) version 2.7. The model was configured with two layers in a domain of 401 × 601 grid points, in which two reservoirs were separated by a channel 200 grid points along with a minimum width of 41 grid points. As in the laboratory experiments, the curvature of the channel sides was 2.5 times the minimum channel width.

The initial state was one of the motionless flow with the interface set to $0.95H$ in the right-hand reservoir and $0.05H$ in the left-hand reservoir. The transition from one height to the other occurred in a region of half-width five grid points. The midpoint

of this region is equivalent to the barrier in the experiments. Except where otherwise stated the barrier was located at the center of the channel. The time step, Δt, and horizontal resolution, Δx, were chosen so that $\sqrt{g'H}\Delta t/\Delta x < 0.1$.

Either a free slip or a no-slip boundary condition was applied on the side walls. The Ekman number, E_W based on the channel width, W, and the horizontal viscosity, ν_E, was of the order of 10^{-4}, comparable to the small-scale experiments, and a factor of 10 greater than in the Coriolis experiments. A quadratic bottom drag was applied in the lower layer for some of the experiments. For a velocity $\sim\sqrt{g'H}$ the equivalent Ekman number is of the order of $E_N = (0.25 c_d B_u W/H)^2$, where c_d is the drag coefficient. This equivalent Ekman number was set to be $\sim 5\times 10^{-3}$ or $\sim 5\times 10^{-4}$.

Appendix D. Theoretical solution for exchange through a contraction

In hydraulic problems it is usual to consider the flow to be slowly varying in the along-channel direction so that semi-geostrophic theory may be applied, to be inviscid and to be hydrostatic (e.g. Pratt and Armi, 1990; Dalziel, 1990; Hunkins and Whitehead, 1992). Here we make the additional assumptions that the channel is of uniform depth and that the potential vorticity in each layer is uniform and set by the depth of the reservoirs. We present the resulting equations in non-dimensional form with lengths non-dimensionalized by $R/\sqrt{2}$, where $R = (g'H)^{1/2}/f$, depths by H, velocities by $fR/\sqrt{2}$. The cross-channel momentum equations are assumed to be geostrophic

$$u_1 = -\frac{\partial p}{\partial y},$$

$$u_2 = -\frac{\partial p}{\partial y} - 2\frac{\partial h_2}{\partial y}, \tag{16}$$

and conservation of potential vorticity implies

$$\frac{\partial u_1}{\partial y} = \frac{h_1}{H} + 1,$$

$$\frac{\partial u_2}{\partial y} = \frac{h_2}{H} + 1. \tag{17}$$

Conservation of Bernoulli potential along streamlines (ψ_i) can be expressed as

$$\tfrac{1}{2}u_1^2 + p = B_1(\psi_1),$$

$$\tfrac{1}{2}u_2^2 + p + 2h_2 = B_2(\psi_2). \tag{18}$$

Combining (16) and (17) we find that

$$\frac{\partial^2 h_2}{\partial y^2} - h_2 + \frac{1}{2} = 0, \tag{19}$$

which has solutions

$$h_2 = \tfrac{1}{2} + A\sinh y + B\cosh y,$$

$$u_1 = C + \frac{y}{2} + (A\sinh y + B\cosh y),$$

$$u_2 = C + \frac{y}{2} - (A\sinh y + B\cosh y). \tag{20}$$

We will assume that $0 < h_2 < 1\ \forall y$ (i.e. both layers remain attached to both boundaries). We may now calculate the volume flux in each layer

$$\begin{aligned} Q_1 = &\int_{-W/2}^{W/2} \mathrm{d}y u_1(1-h_2) \\ = &-AB\sinh w \\ &+ A\left(2\sinh\frac{W}{2} - \frac{W}{2}\cosh\frac{W}{2}\right) \\ &+ C\left(\frac{W}{2} - 2B\sinh\frac{W}{2}\right), \end{aligned} \tag{21}$$

and

$$\begin{aligned} Q_2 = &\int_{-W/2}^{W/2} \mathrm{d}y u_2 h_2 \\ = &-AB\sinh w \\ &- A\left(2\sinh\frac{W}{2} - \frac{W}{2}\cosh\frac{W}{2}\right) \\ &+ C\left(\frac{W}{2} + 2B\sinh\frac{W}{2}\right). \end{aligned} \tag{22}$$

Making the additional assumption of no net flux so that

$$Q_1 + Q_2 = 0, \tag{23}$$

it can be shown that

$$C = -\frac{2}{W}AB\sinh W, \tag{24}$$

so that

$$\begin{aligned} Q_2 = -Q_1 = Q = &-A\left(2\sinh\frac{W}{2} - \frac{W}{2}\cosh\frac{W}{2}\right) \\ &+ AB^2\frac{4}{W}\sinh W\sinh\frac{W}{2}. \end{aligned} \tag{25}$$

The exchange flux Q is independent of x. We can derive one further conserved quantity by noting that the boundary $y = W/2$ is a streamline for both

layers and so taking the difference of 18 we find

$$\Delta B = \tfrac{1}{2}u_2^2 - \tfrac{1}{2}u_1^2 + 2h_2. \tag{26}$$

is also independent of x on $y = W/2$.

The flow will be critical if

$$\begin{vmatrix} \dfrac{\partial Q}{\partial A} & \dfrac{\partial Q}{\partial B} \\ \dfrac{\partial \Delta B}{\partial A} & \dfrac{\partial \Delta B}{\partial B} \end{vmatrix} = 0 \tag{27}$$

(see e.g. Pratt and Helfrich, 2005). We now make the additional assumptions that the flow is critical at the narrowest section and that by symmetry $B = 0$ at this section. It is seen from 25 that $\partial Q/\partial B = 0$ when $B = 0$, therefore for 27 to be satisfied $\partial \Delta B/\partial B = 0$ (in general $\partial Q/\partial A \neq 0$). This can be expressed as

$$A^2 \frac{8}{W}\cosh^2\frac{W}{2}\sinh\frac{W}{2} - 2\cosh\frac{W}{2} + \frac{W}{2}\sinh\frac{W}{2} = 0. \tag{28}$$

This equation was solved to find A for each value of W and the flux was then determined from 25. Note that $Bu = \sqrt{2}/W$. The results were calculated down to the value ($\simeq 0.87$) of Bu at which the interface is predicted to separate from the side wall. However, at $Bu = 0.87$ the solution predicts that there is a maximum in the non-dimensional flux and that the flux decreases as B_u decreases below 0.87 (i.e. as the channel width increases). Therefore, in Fig. 10 solutions are shown only for $Bu > 0.87$. Hunkins and Whitehead (1992) presented a similar solution. However, instead of the hydraulic control condition they used an approximate energy balance. This theory predicted the boundary between separated and unseparated flows to be at $Bu \simeq 0.27$ for which the non-dimensional flux was predicted to 0.156. This solution may be extended to higher Burger numbers (by changing the right-hand side of their equation (31) to values less than $H/2$). However, the resulting solution does not exhibit reasonable behavior for large values of B_u.

References

Anati, D., Assaf, G., Thompson, R., 1977. Laboratory models of sea straits. Journal of Fluid Mechanics 81, 341–351.

Armi, L., 1986. The hydraulics of two flowing layers with different densities. Journal of Fluid Mechanics 163, 27–58.

Astraldi, M., Balopoulos, S., Candela, J., Font, J., Gacic, M., Gasparini, G.P., Manca, B., Theocharis, A., Tintore, J., 1999. The role of straits and channels in understanding the characteristics of Mediterranean Circulation. Progress in Oceanography 44, 65–108.

Beranger, K., Mortier, L., Gassparini, G.P., Gervasio, L., Astraldi, M., Crepon, M., 2004. The dynamics of the Sicily Strait: a comprehensive study from observations and models. Deep-Sea Research II 51 (4–5), 411–440.

Bigg, G.R., Jickells, T.D., Liss, P.S., Osborn, T.J., 2003. The role of the oceans in climate. International Journal of Climatology 23 (10), 1127–1159.

Bleck, R., Boudra, D., 1986. Wind-driven spin-up in eddy-resolving ocean models formulated in isopycnic and isobaric coordinates. Journal of Geophysical Research 91, 7611–7621.

Bleck, R., Boudra, D., 1990. A wind-driven isopycnic coordinate model of the north and equatorial Atlantic-ocean. 1. Model development and supporting experiments. Journal of Geophysical Research 95, 3273–3285.

Bryden, H.L., Candela, J., Kinder, T.H., 1994. Exchange through the Strait of Gibraltar. Progress in Oceanography 33, 201–248.

Cenedese, C., Dalziel, S.B., 1998. Concentration and depth fields determined by the light transmitted through a dyed solution. In: Carlomagno, G.M., Grant, I. (Eds.), Proceedings of the Eighth International Symposium on Flow Visualization. ISBN-0-9533991-0, paper 061.

Dalziel, S.B., 1988. Two-layer hydraulics: maximal exchange flows. Ph.D. Thesis, Department of Applied Mathematics and Theoretical Physics, University of Cambridge, see also ⟨http://www.damtp.cam.ac.uk/lab/people/sd103/papers/1988/Thesis_Dalziel.pdf⟩.

Dalziel, S.B., 1990. Rotating two-layer sill flows. In: Pratt, L.J. (Ed.), The Physical Oceanography of Sea Straits. Kluwer Academic, Dordrecht, pp. 343–371.

Dalziel, S.B., 1991. Two-layer hydraulics: a functional approach. Journal of Fluid Mechanics 223, 135–163.

Dalziel, S.B., 1992a. DigImage: system overview. Cambridge Environmental Research Consultants, Ltd., 43pp.

Dalziel, S.B., 1992b. Maximal exchange in channels with nonrectangular cross-sections. Journal of Physical Oceanography 22 (10), 1188–1206.

Fincham, A., Delerce, G., 2000. Advanced optimization of correlation imaging velocimetry algorithms. Experiments in Fluids, S13–S22.

Fincham, A.M., Spedding, G.R., 1997. Low cost, high resolution dpiv for measurement of turbulent fluid flow. Experiments in Fluids 23, 449–462.

Fristedt, T., Hietala, R., Lundberg, P., 1999. Stability properties of a barotropic surface-water jet observed in the Denmark Strait. Tellus Series A 51 (5), 979–989.

Fritsch, F.N., Carlson, R.E., 1980. Monotone piecewise cubic interpolation. SIAM Journal of Numerical Analysis 17, 238–246.

Gill, A.E., 1976. Adjustment under gravity in a rotating channel. Journal of Fluid Mechanics 77 (3), 603–627.

Gill, A.E., 1977. The hydraulics of rotating-channel flow. Journal of Fluid Mechanics 80, 641–671.

Greenspan, H.P., 1968. The Theory of Rotating Fluids. Cambridge University Press, Cambridge.

Griffiths, R.W., Hopfinger, E.J., 1983. Gravity currents moving along a lateral boundary in a rotating fluid. Journal of Fluid Mechanics 134, 357–399.

Helfrich, K.R., 1995. Time-dependent two-layer exchange flows. Journal of Physical Oceanography 25, 359–373.

Helfrich, K.R., Kuo, A.C., Pratt, L.J., 1999. Nonlinear Rossby adjustment in a channel. Journal of Fluid Mechanics 390, 187–222.

Hermann, A.J., Rhines, R.P., Johnson, E.R., 1989. Nonlinear Rossby adjustment in a channel: beyond Kelvin waves. Journal of Fluid Mechanics 205, 469–502.

Hogg, A.M., Ivey, G.N., Winters, K.B., 2001. Hydraulics and mixing in controlled exchange flows. Journal of Geophysical Research 106 (C1), 959–972.

Holford, J.M., Dalziel, S.B., 1996. Measurements of layer depth in a two-layer flow. Applied Scientific Research 56 (2–3), 191–207.

Hunkins, K., Whitehead, J.A., 1992. Laboratory simulation of exchange through Fram Strait. Journal of Geophysical Research 97, 11299–11321.

Jia, Y.L., 2000. Formation of an Azores Curent due to Mediterranean overflow in a modeling study of the North Atlantic. Journal of Physical Oceanography 30 (9), 2342–2358.

Johnson, G.C., Ohlsen, D.R., 1994. Frictionally modified rotating hydraulic channel exchange and ocean outflows. Journal of Physical Oceanography 24, 66–78.

Kahaner, D., Moler, C., Nash, S., 1988. Numerical Methods and Software. Prentice-Hall, Englewood Cliffs, NJ.

Käse, R.H., Girton, J.B., Sanford, T.B., 2003. Structure and variability of the Denmark Strait overflow: model and observations. Journal of Geophysical Research 108(C6), art. 3181.

Killworth, P., 1995. Hydraulic control and maximal flow in rotating stratified hydraulics. Deep-Sea Research I 42 (6), 859–871.

Lane-Serff, G.F., Smeed, D.A., Postlethwaite, C.R., 2000. Multi-layer hydraulic exchange flows. Journal of Fluid Mechanics 416, 269–296.

Pratt, L., Armi, L., 1990. Two-layer rotating hydraulics: strangulation, remote and virtual controls. PAGEOPH 133 (4), 587–617.

Pratt, L.J., 2004. Recent progress on understanding the effects of rotation in models of sea straits. Deep-Sea Research II 51 (4–5), 351–369.

Pratt, L.J., Helfrich, K., 2005. Generalized conditions for hydraulic criticality of oceanic overflows. Journal of Fluid Mechanics 35, 1782–1800.

Reid, J.L., 1994. On the total geostrophic circulation of the North-Atlantic ocean-flow patterns, tracers and transports. Progress in Oceanography 33 (1), 1–92.

Riemenschneider, U., Smeed, D.A., Killworth, P.D., 2005. Theory of two-layer hydraulic exchange. Journal of Fluid Mechanics 545, 373.

Serra, N., Sadoux, S., Ambar, I., Renouard, D., 2002. Observations and laboratory modeling of meddy generation at Cape St. Vincent. Journal of Physical Oceanography 32, 3–25.

Smeed, D.A., 2000. Hydraulic control in three-layer exchange flows and application to the Bab al Mandab. Journal of Physical Oceanography 30 (10), 2574–2588.

Smith, P.C., 1976. Baroclinic instability in the Denmark Strait overflow. Journal of Physical Oceanography 6, 355–371.

Stansfield, K., Smeed, D.A., Gasparini, G.P., McPhail, S., Millard, N., Tevenson, P., Webb, A., Vetrano, A., Rabe, B., 2001. Deep-sea, high-resolution, hydrography and current measurements using an autonomous underwater vehicle: the overflow from the Strait of Sicily. Geophysical Research Letters 28 (13), 2645–2648.

Stansfield, K., Gasparini, G.P., Smeed, D.A., 2003. High-resolution observations of the path of the overflow from the Strait of Sicily. Deep-Sea Research I 50, 1129–1149.

Stenström, P., 2003. Mixing and recirculation in two-l ayer exchange flows. Journal of Geophysical Research 108 (C8).

Stern, M.E., 2004. Local "mean field" theory of hydraulically controlled strait flow. Journal of Physical Oceanography 34, 1692–1701.

Timmermanns, M.-L.E., Pratt, L.J., 2005. Two-layer rotating exchange flow between two deep basins: theory and application to the Strait of Gibraltar. Journal of Physical Oceanography 35, 1568–1592.

Tritton, D.J., 1988. Physical Fluid Dynamics, second ed. Clarendon Press, Oxford.

Whitehead, J.A., Miller, A.R., 1979. Laboratory simulation of the gyre in the Alboran Sea. Journal of Geophysical Research 84, 3733–3742.

Whitehead, J.A., Leetmaa, A., Knox, R.A., 1974. Rotating hydraulics of strait and sill flows. Geophysical Fluid Dynamics 6, 101–125.

Winters, K.B., Seim, H.E., 2000. The role of dissipation and mixing in exchange flow through a contracting channel. Journal of Fluid Mechanics 407, 265–290.

Zaremba, L.J., Lawrence, G.A., Pieters, R., 2003. Frictional two-layer exchange flow. Journal of Fluid Mechanics 474, 339–354.